Research Square

Preprints are preliminary reports that have not undergone peer review.
They should not be considered conclusive, used to inform clinical practice,
or referenced by the media as validated information.

Local structural modifications and excitation-dependent photoluminescence in Tb3+-doped Na0.5Bi0.5TiO3 ceramics

T.A Tran
Ho Chi Minh City University of Technology and Engineering
L.S. Hai
Ho Chi Minh City University of Technology and Engineering
Thanh Son L.V
Trường Đại học Sư phạm – Đại học Đà Nẵng
Khan D.T
Trường Đại học Sư phạm – Đại học Đà Nẵng
Chinh N.B.V.
Trường Đại học Sư phạm – Đại học Đà Nẵng
Lien Phan
Trường Đại học Sư phạm – Đại học Đà Nẵng
Truong Son L.V.
Trường Đại học Sư phạm – Đại học Đà Nẵng
Thanh-Thao T.T
Hue University
Hoang T.P.
Duy Tan University
Hong Van Truong
Duy Tan University
Jabbarov R.B.
Ministry of Science and Education Republic of Azerbaijan
Jabarov S.H.
Ministry of Science and Education Republic of Azerbaijan
Aliyev Y.I.
Azerbaijan State Pedagogical University
Dat T.N.
tndat@ued.udn.vn

Trường Đại học Sư phạm – Đại học Đà Nẵng

Research Article

Keywords: NBT, Rhombohedral symmetry, photoluminescence, Tb3+

Posted Date: November 26th, 2026

DOI: https://doi.org/10.21203/rs.3.rs-11416417/v1

License: This work is licensed under a Creative Commons Attribution 4.0 International License.
Read Full License

Additional Declarations: No competing interests reported.

Local structural modifications and excitation-dependent photoluminescence in Tb^{3+}-doped $Na_{0.5}Bi_{0.5}TiO_3$ ceramics

T.A. Tran[1], L.S. Hai[1], L.V. Thanh Son[2], D.T. Khan[2], N.B.V. Chinh[2], P. Lien[2], L.V. Truong Son[2], T.T. Thanh-Thao[3], T.P. Hoang[4,5*], H.V. Truong[4,5], R.B. Jabbarov[6], S.H. Jabarov[6], Y.I. Aliyev[7], T.N. Dat[2*]

[1] Department of Engineering Physics, Hochiminh City University of Technology and Engineering, 700000 Ho Chi Minh City, Vietnam

[2] The University of Danang - University of Science and Education, 550000 Danang, Vietnam

[3] Faculty of Electronics, Electrical Engineering and Material Technology, University of Sciences, Hue University, 530000 Hue, Vietnam

[4] Institute of Research and Development, Duy Tan University, 550000 Danang, Vietnam

[5] Faculty of Environmental and Natural Sciences, Duy Tan University, 550000 Danang, Vietnam

[6] Institute of Physics, Ministry of Science and Education Republic of Azerbaijan, AZ-1143 Baku, Azerbaijan

[7] Azerbaijan State Pedagogical University, AZ-1000 Baku, Azerbaijan

[*] Corresponding authors: T.P. Hoang (hoangtrongphuc@duytan.edu.vn); T.N. Dat (tndat@ued.udn.vn)

Abstract

Lead-free $Na_{0.5}(Bi_{1-x}Tb_x)_{0.5}TiO_3$ ceramics (x = 0 to 0.08) were prepared by solid-state reaction to follow how A-site Tb^{3+} reshapes the lattice, phonons and emission. Rietveld refinement shows that the average rhombohedral R3c structure is retained, with a minor pyrochlore impurity at higher x. As Tb^{3+} (1.24 Å) is smaller than Bi^{3+} (1.32 Å), the cell volume shrinks from 351.765 to 349.731 $Å^3$, while the tolerance factor barely moves (0.972 to 0.970). Raman spectra suggest a local response: the Na-O/Bi-O mode intensity ratio falls and the TiO_6 bands shift, yet no new modes appear. EDS confirms the presence of Tb, and the mean grain size drops from 1.7 to 1.2 μm. Excitation spectra show a strong $^7F_6 \rightarrow {}^5D_4$ line at 488 nm and a weak band at 378 nm ($^7F_6 \rightarrow {}^5G_6/{}^5D_3$). Under 378 nm, which can also excite the host, a broad host-related blue band accompanies the Tb^{3+} lines, giving blue light at CIE (x, y) ≈ (0.20, 0.23). Under 488 nm, below the host absorption edge, only Tb^{3+} is excited and the emission is green, (0.35, 0.63). Tb^{3+} emission is strongest at x = 0.02. This suggests potential for excitation-selective optical tagging.

Keywords NBT · Rhombohedral symmetry · photoluminescence · Tb^{3+}

1 Introduction

Perovskite oxides ABO_3 have long served as cornerstone materials in modern technology due to their remarkable chemical flexibility, structural versatility, and wide spectrum of physical properties, rendering them highly attractive for optoelectronic devices, sensors, and energy storage systems [1]. Among these, lead zirconate titanate $Pb(Zr,Ti)O_3$ (PZT)-based ceramics have historically dominated the ferroelectric and piezoelectric markets. However, the high toxicity and environmental volatility of Pb during high-temperature processing have triggered stringent global environmental regulations, driving an urgent quest for environmentally friendly lead-free alternatives. Sodium bismuth titanate $Na_{0.5}Bi_{0.5}TiO_3$ (NBT) has emerged as one of the most promising lead-free candidates owing to its strong ferroelectric response, characterized by a large remnant polarization $P_r \sim 38 \mu C/cm^2$ and a high Curie temperature $T_C \sim 320°C$ [2].

From a structural perspective, NBT represents a classic A-site disordered perovskite where the A-sublattice is randomly shared by univalent Na^{+} and trivalent Bi^{3+} cations [3, 4]. The presence of the lone $6s^2$ electron pair in Bi^{3+} plays a pivotal role in inducing ferroelectric polarization through strong Bi 6s - O 2p orbital hybridization [4]. Crucially, this intrinsic A-site disorder and the similar ionic radius of Bi^{3+} render NBT an exceptional crystalline host matrix for trivalent rare earth RE^{3+} dopant. The substitution of RE^{3+} ions into the A-site can be readily accommodated without inducing severe lattice instability, offering a versatile platform for structural engineering and defect control [5]. The integration of RE^{3+} activators into ferroelectric hosts opens fascinating avenues for developing multifunctional optical-electrical materials. Rare-earth cations possess shielded intra-4f electronic transitions 4f-4f, yielding sharp emission lines, high quantum efficiency, and excellent color purity [6–8]. Among various RE^{3+} dopants, Tb^{3+} is particularly attractive due to its intense green emission originating from the $^5D_4 \rightarrow {}^7F_5$ transition (~545 nm). Furthermore, the luminescent behavior of Tb^{3+} is highly sensitive to variations in local crystal field symmetry, making it an effective luminescent probe for monitoring local structural modifications [9].

Tb^{3+} doping of NBT is not without precedent: Swain et al. reported the structural, dielectric, and optical properties of $(Tb_xBi_{1-x})_{0.5}Na_{0.5}TiO_3$ for x up to 0.03 [9], while Jeshurun et al. examined (Y^{3+}, Tb^{3+})-codoped NBT nanoparticles with Tb-related green emission at compositions overlapping the higher end of the present series (x = 0.04–0.08) [10]. These studies did not specifically examine how the excitation wavelength determines the relative contributions of host-related and Tb^{3+}-centered emission, or how the resulting emission color evolves with Tb content in a singly Tb^{3+}-doped NBT host across a broad composition range. Despite growing interest in RE^{3+} modified NBT systems, a comprehensive understanding of how Tb^{3+} incorporation influences crystal structure, local symmetry perturbations, and photoluminescence mechanisms remains crucial for tailoring multifunctional performance. In this work, a series of Tb^{3+} doped NBT ceramics $Na_{0.5}(Bi_{1-x}Tb_x)_{0.5}TiO_3$ were synthesized via a conventional solid-state reaction route. The structural evolution, local site symmetry, and detailed photoluminescence excitation and emission (PLE/PL) dynamics were systematically investigated. In particular, this work examines the concentration dependence of the lattice contraction and local vibrational (Raman) response upon Tb^{3+} substitution, the excitation pathways of Tb^{3+} under 378 and 488 nm excitation, and the resulting excitation-dependent balance between host-related blue emission and Tb^{3+}-centered green emission in a singly Tb^{3+}-doped NBT host. This study provides fundamental insights into Tb^{3+} doped NBT systems and highlights their potential for excitation tunable luminescent applications.

2 Experiment details

$Na_{0.5}(Bi_{1-x}Tb_x)_{0.5}TiO_3$ materials with x = 0.00, 0.02, 0.04, 0.06, 0.08, designated as NBT0, NBT2, NBT4, NBT6, and NBT8, respectively, were synthesized by the solid-state reaction method. Precursors including Na_2CO_3 (99%), Bi_2O_3 (99%), TiO_2 (99.9%), and Tb_2O_3 (99.9%) were used for the material synthesis. The precursors were weighed in exact stoichiometric proportions and ground in an agate mortar using absolute ethanol (99%) as the solvent for 1 h. Subsequently, the mixture was calcined at 800°C for 2 h in air. Next, the mixture was re-ground and pressed into pellets with a diameter of 10 mm under a pressure of 1.5 tons. Finally, the materials were sintered at 1100°C for 3 h with a heating rate of 3 °C/min. Phase analysis of the materials was conducted using X-ray diffraction (D8 Advance Eco, Bruker) in the 2θ range from 20 to 80° at room temperature using Cu Kα radiation (λ = 1.5406 Å). The surface morphology of the materials was analyzed by scanning electron microscopy (SEM) using a JEOL JSM IT-200 system. The structure of the materials was analyzed using Raman scattering spectroscopy with a

532nm laser on an Xplora Plus system (Horiba). The photoluminescence properties of the materials were investigated using an FL3-22C fluorescence spectrophotometer (Horiba) equipped with a 450 W Xenon lamp. All measurements were performed under ambient conditions.

3 Results and discussion

Figure 1(a) shows the X-ray diffraction (XRD) patterns of the $Na_{0.5}(Bi_{1-x}Tb_x)_{0.5}TiO_3$ samples with x = 0–0.08, recorded over the 2θ range of 20°–80°. The diffraction patterns are characteristic of the perovskite NBT phase, with prominent reflections located at approximately 22°, 32°, 40°, 47°, 58°, 68°, and 77°, which are indexed to the (100), (110), (111), (200), (211), (220), and (221) planes, respectively [11]. As shown in Fig. 1(b), the most intense (110) reflection progressively shifts toward higher 2θ values with increasing Tb content. According to Bragg's law, this shift indicates a reduction in the corresponding interplanar spacing and is consistent with lattice contraction induced by the substitution of smaller Tb^{3+} ion (1.24 Å) for Bi^{3+} ion (1.32 Å) at the A site [1, 12]. Rietveld refinements of the XRD patterns were performed using the FullProf package with a rhombohedral structural model described by the R3c space group. The calculated profiles reproduce the experimental diffraction patterns well (See Table 1).

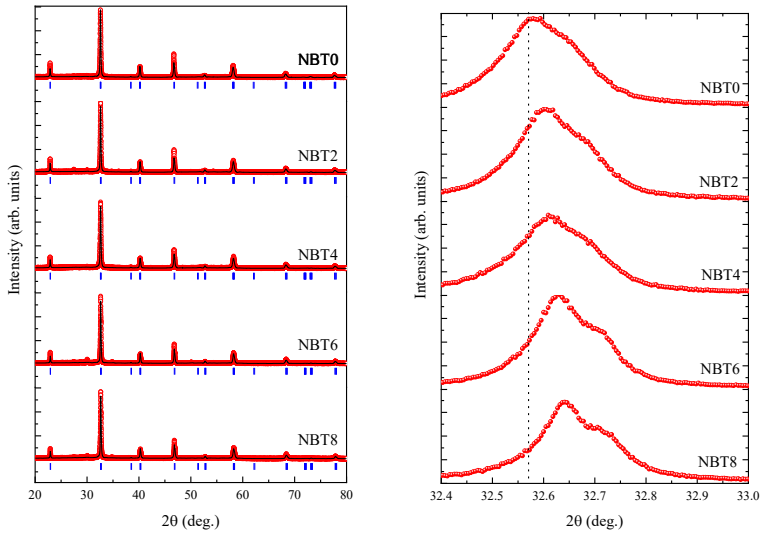


Fig. 1 (a) XRD patterns of NBT0–NBT8 at room temperature (symbols: observed data; solid lines: calculated profiles; vertical ticks: Bragg positions); (b) Magnified view of the (110) reflection showing its systematic shift with increasing Tb^{3+} content

Rietveld refinements were performed for all compositions, and the resulting structural parameters and reliability factors are summarized in Table 1. All refinement reliability factors remain below 5%, indicating that the rhombohedral R3c model provides a satisfactory description of the average crystal structure over the investigated composition range. For the undoped sample ($Na_{0.5}Bi_{0.5}TiO_3$), Na and Bi atoms occupy the *6a* position at *(0, 0, 0.26270)*, Ti is located at *6a (0, 0, 0.00630)*, and O is positioned at *18b (0.12600, 0.33600, 0.08330)*. With increasing Tb content, weak additional reflections emerge near 2θ ≈ 30°. These reflections are tentatively assigned to a minor $Bi_2Ti_2O_7$ pyrochlore secondary phase (PDF No. 32-0118) [13], which may be associated with local compositional inhomogeneity during synthesis. Nevertheless, the dominant diffraction features remain well

described by the R3c model, indicating that the average rhombohedral perovskite framework is retained throughout the investigated Tb-substitution range.

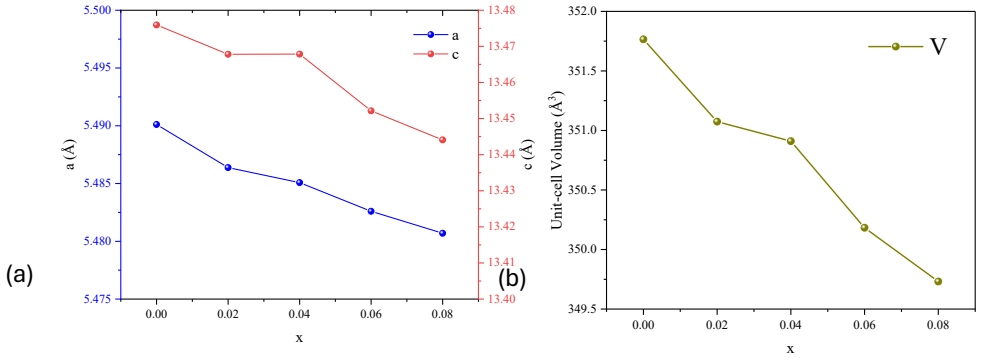


Fig. 2 Unit-cell parameters (a) and Unit-cell volume (b) of NBT0 → NBT8

The refined lattice parameters of the rhombohedral phase are also listed in Table 1 and plotted in Fig.2. Both lattice constants *a* and *c*, as well as the unit-cell volume, decrease systematically with increasing Tb concentration, consistent with previous reports [6]. The structural evolution can also be considered in terms of the Goldschmidt tolerance factor $t = (r_A + r_O)/ [\sqrt{2}(r_B + r_O)]$. Using r_{Na} = 1.39 Å, $r_{Bi^{3+}}$ = 1.32 Å, $r_{Tb^{3+}}$ = 1.24 Å (commonly adopted values for 12-fold coordination), $r_{Ti^{4+}}$ = 0.605 Å for sixfold coordination and $r_{O^{2-}}$ = 1.40 Å, the calculated tolerance factor decreases only slightly from approximately 0.972 for (x=0) to 0.970 for (x=0.08). The small variation in *t* indicates that Tb substitution introduces only a modest geometrical perturbation to the perovskite lattice, consistent with the retention of the average rhombohedral framework. However, it should be emphasized that the tolerance factor provides only a geometrical criterion for perovskite stability and does not, by itself, determine the crystallographic space group.

The surface morphology and grain-size evolution of the $Na_{0.5}(Bi_{1-x}Tb_x)_{0.5}TiO_3$ ceramics were examined by scanning electron microscopy (SEM), as shown in Fig. 3. The SEM image of the undoped $Na_{0.5}Bi_{0.5}TiO_3$ ceramic reveals a dense microstructure composed predominantly of well-developed, nearly equiaxed polygonal grains with clearly defined grain boundaries. The grain-size distribution is relatively narrow, with most grains lying in the range of approximately 1–2.5 μm and an average grain size of about 1.7 μm. The Tb-substitution induces almost no noticeable change in the grain morphology of $Na_{0.5}(Bi_{1-x}Tb_x)_{0.5}TiO_3$ system. Quantitative analysis of the SEM images reveals a systematic decrease in the average grain size from approximately 1.7 μm for the undoped sample to approximately 1.2 μm at the highest Tb concentration. The progressive grain refinement suggests that Tb^{3+} substitution suppresses grain growth during sintering. Such behavior may arise from Tb-induced modifications of defect chemistry and grain-boundary mobility [9, 10].

Table 1 Structural parameters obtained by Rietveld refinement

Parameters	Samples				
	NBT	NBT2	NBT4	NBT6	NBT8
a (Å)	5.49011	5.48638	5.48508	5.48260	5.48070
c (Å)	13.47593	13.46780	13.46785	13.45214	13.44408
c/a	2.45	2.45	2.46	2.45	2.45
V ($Å^3$)	351.765	351.074	350.910	350.183	349.731
R_b (%)	3.54	4.10	2.69	3.28	2.99
R_f (%)	2.54	2.47	2.25	2.65	2.61

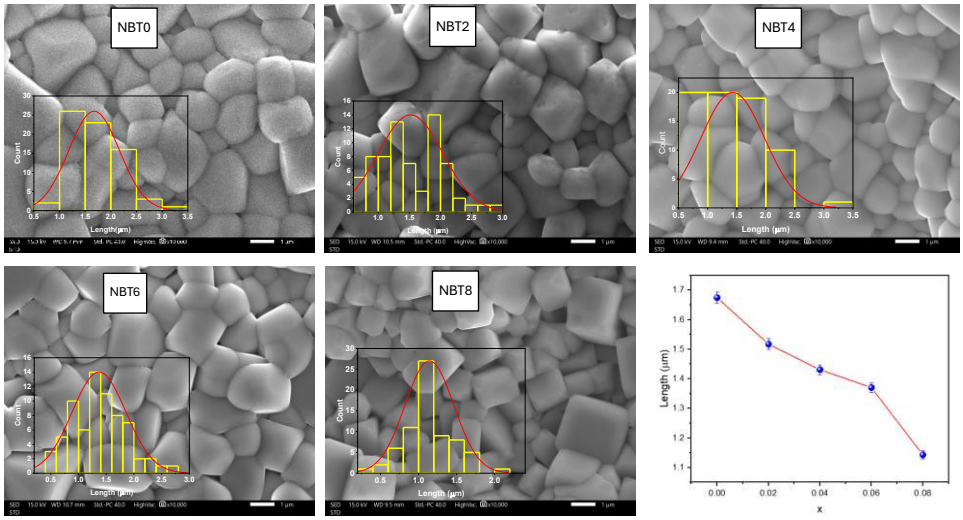


Fig. 3 SEM images of NBT0→ NBT8 samples, along with the grain size distributions of the materials

Energy-dispersive X-ray spectroscopy (EDS) was employed to examine the elemental composition. Representative EDS spectra for the x = 0 and x = 0.08 compositions are shown in Fig. 4. The undoped NBT sample exhibits peaks corresponding to Na, Bi, Ti, and O, with no detectable Tb signal. In the Tb-substituted samples, additional Tb peaks are clearly observed, confirming the presence of Tb in the ceramics. The quantitative EDS results for all studied samples are summarized in Table 2. The EDS results verify the presence of Na, Bi, Ti, O, and Tb in the doped samples and are qualitatively consistent with the nominal composition of the $Na_{0.5}(Bi_{1-x}Tb_x)_{0.5}TiO_3$ system. Given the semiquantitative nature of EDS, particularly for light elements such as O and Na, small deviations from the nominal stoichiometry are expected. In particular, NBT4 shows a noticeably lower Ti and higher O content than the other samples, so Table 2 is used here only to confirm the presence of the constituent elements and not to determine the stoichiometry.

Table 2 Elemental composition of NBT samples (%atom)

Sample	Na	Bi	Ti	O	Tb
NBT0	7.85±0.21	9.70±0.11	16.51±0.26	65.94±0.83	nd
NBT2	8.01±0.12	9.36±0.07	16.04±0.15	66.38±0.48	0.22±0.03
NBT4	8.41±0.13	8.17±0.06	11.45±0.16	71.67±0.49	0.30±0.03
NBT6	8.19±0.11	9.09±0.06	15.21±0.13	67.10±0.42	0.41±0.03
NBT8	7.83±0.13	9.36±0.07	16.25±0.16	66.01±0.51	0.55±0.04

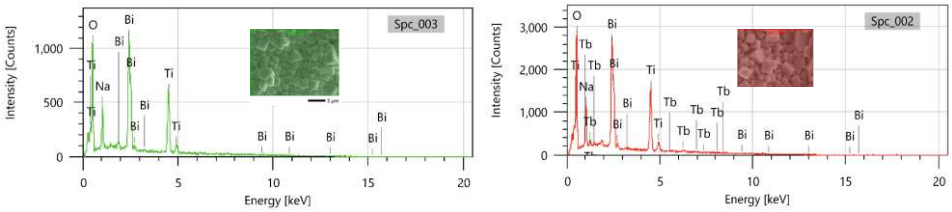


Fig. 4 Energy-dispersive X-ray spectroscopy (EDS) spectra of the NBT0 (a) and NBT8 (b) samples

Raman spectra were recorded over the range of 50–1000 cm^{-1} using a Horiba XploRA PLUS spectrometer equipped with a 532-nm excitation laser and an 1800-grooves/mm grating. For the rhombohedral R3c structure, group-theoretical analysis predicts 13 Raman-active phonon modes, 4A1 + 9E [3, 14]. In practice, however, fewer modes are resolved experimentally. This reduction can arise from the overlap or near degeneracy of closely spaced phonon modes, as well as from the weak Raman scattering intensity of modes with small polarizability derivatives. Additional spectral broadening associated with structural disorder may further hinder the resolution of individual Raman modes.

Table 3 Raman modes of the NBT samples obtained by deconvoluting their Raman spectra

Raman modes (cm-1)	NBT0	NBT2	NBT4	NBT6	NBT8
$A_1(TO_1)$	69.97	72.45	72.68	73.04	73.05
$A_1(TO_1)$	131.54	133.61	133.35	132.45	129.38
$E(TO_2)$	271.54	270.97	268.98	266.76	260.75
$E(LO_2)$	517.29	518.69	520.97	519.68	522.24
$E(LO_2)$	587.68	588.44	588.56	588.69	588.96
	744.80	745.77	752.13	754.11	754.39
	824.43	830.39	830.82	825.94	820.21

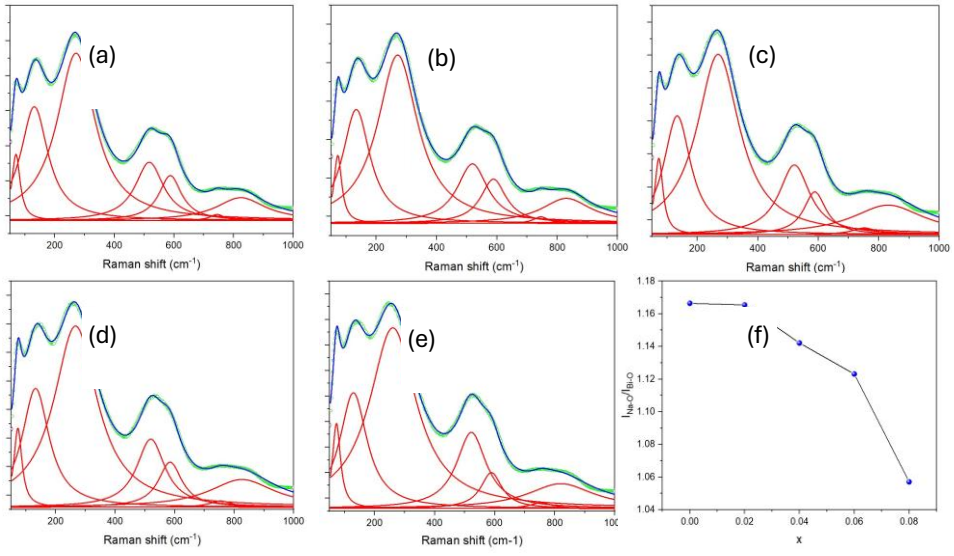


Fig. 5 (a)→(e)Deconvolution Raman spectra of NBT0 and Raman spectra of NBT0 → NBT8 samples, (f) The intensity ratio of the Na-O vibration mode to the Bi-O vibration mode

Figures 5(a)–5(e) show the Raman spectra of the $Na_{0.5}(Bi_{1-x}Tb_x)_{0.5}TiO_3$ samples together with their decomposition into individual Lorentzian components. Five characteristic spectral regions can be distinguished: (i) a low-frequency mode near 68 cm^{-1}, (ii) a mode near 131 cm^{-1}, (iii) a broad band centered at approximately 270

cm^{-1}, (iv) a broad spectral region extending from approximately 430 to 650 cm^{-1}, and (v) a high-frequency band near 815 cm^{-1}. The low-frequency peaks near 68 and 131 cm^{-1} are assigned to $A_1(TO_1)$-type A-site vibrations, dominated by Bi–O and Na–O motions, respectively [3]. The intensity ratio between the Na–O- and Bi–O-related modes, ($I_{Na\text{-}O}/I_{Bi\text{-}O}$), decreases systematically with increasing Tb content, as shown in Fig. 5(f). This evolution suggests a progressive modification of the local A-site vibrational environment induced by Tb^{3+} substitution for Bi^{3+}. Such changes may arise from local strain, cation disorder, and/or altered A-site bonding induced by Tb^{3+} incorporation. The broad band centered near 270 cm^{-1} is associated with the $E(TO_2)$ mode involving Ti–O vibrations. The features in the 430–650 cm^{-1} region originate from symmetric vibrations of the TiO_6 octahedra. These modes are used to identify the phase transition in ferroelectrics of perovskite structure because it relate to polar Ti-cation displacement and octahedral-tilt distortion [15, 16]. The high-frequency band near 815 cm^{-1} is assigned to an LO-type mode associated with asymmetric breathing vibrations of the TiO_6 octahedra.

With increasing Tb concentration, the mid-frequency band exhibits a shift toward lower wavenumber ($E(TO_2)$: 271.5 → 260.8 cm^{-1}), whereas several higher-frequency bands shift toward higher wavenumber. This contrasting behavior is consistent with local lattice distortions induced by the substitution of the smaller Tb^{3+} ion for Bi^{3+} at the A site. The resulting contraction of the local A-site environment can modify Ti–O bond lengths and TiO_6 octahedral tilting, thereby affecting the different Raman modes in distinct ways. Despite these systematic frequency shifts, the overall Raman spectral profile remains essentially unchanged across the investigated composition range, with no additional modes or abrupt spectral changes. This behavior is consistent with the retention of the average rhombohedral R3c framework inferred from the XRD analysis and agrees with previous reports [17].

To clarify the excitation pathways of Tb^{3+} ions in the NBT host, photoluminescence excitation (PLE) spectra were recorded using a FL3-22C spectrofluorometer (Horiba). Figure 6 shows the PLE spectra of the Tb-substituted samples (x=0.02–0.08), measured over the wavelength range of 300–500 nm while monitoring the characteristic Tb^{3+} green emission at 545 nm. The spectra are dominated by a sharp excitation band centered near 488 nm, assigned to the intra-4*f* transition $^7F_6$ → $^5D_4$ [18]. A much weaker feature near 378 nm is attributed to excitation from the $^7F_6$ ground state to higher lying $^5G_6$ or $^5D_3$ levels [19, 20], from which the excitation relaxes nonradiatively to the emitting $^5D_4$ level. The weaker 378 nm feature may reflect the lower effective excitation strength of these transitions compared with $^7F_6$ → $^5D_4$ at approximately 488 nm under the present experimental conditions. Meanwhile, no pronounced broad excitation band associated with host-lattice absorption or ligand-to-metal charge transfer is resolved within the measured spectral range. Thus, under the present excitation and detection conditions, direct intra-4*f* excitation near 488 nm constitutes the most efficient pumping channel for the Tb^{3+} green emission in the NBT host. Note that 378 nm (3.28 eV) lies close to the optical gap generally reported for NBT-based oxides, so excitation of the host itself at this wavelength cannot be ruled out.

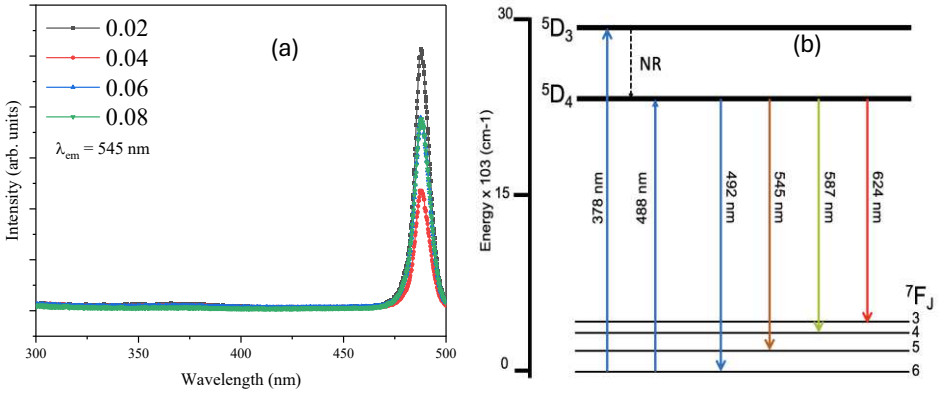


Fig. 6 PLE spectra of NBT2 → NBT8 (a) and energy level transition diagram of Tb^{3+} (b)

To investigate the photoluminescence (PL) properties of $Na_{0.5}(Bi_{1-x}Tb_x)_{0.5}TiO_3$, the emission spectra of the samples were recorded under excitation at 378 nm (400–700 nm range) and 488 nm (range starting above 520 nm), as shown in Fig. 7. As shown in Fig. 7(a), the PL spectrum of the pristine sample under the 378 nm excitation exhibits a broad blue emission band centered at approximately 440–450 nm. It should be noted that undoped NBT is not entirely optically inactive. Volatilization of Na and Bi during high temperature sintering can generates oxygen vacancies and other intrinsic defects, giving rise to a broad defect-related emission band predominantly in the near-UV and blue spectral region [21, 22]. Beside the broaden PL band of the host material, the PL spectra of Tb^{3+} doped samples as excited by 378 nm light contain peaks which correlate to the respective characteristic transitions $^5D_4 \rightarrow {}^7F_6$,(492 nm), $^5D_4 \rightarrow {}^7F_5$ (545 nm), $^5D_4 \rightarrow {}^7F_4$ (587 nm), and $^5D_4 \rightarrow {}^7F_3$(624 nm) of Tb^{3+} ions [23], as shown in Fig. 6(b). In the Tb-doped samples the broad band is stronger than in undoped NBT and its maximum lies at about 440 nm, so a Tb-related modification of the host-related emission, or a weak $^5D_3$-related contribution, cannot be excluded. Under 488 nm excitation, which lies below the host absorption edge, the host-related band is not excited and the spectra consist of the characteristic Tb^{3+} emission lines (Fig. 7(b)), consistent with direct excitation of the $^7F_6 \rightarrow {}^5D_4$ transition (Fig. 6(b)). The intensity of the Tb^{3+} lines is highest for x = 0.02 and lower for higher Tb contents, although the trend is not strictly monotonic (Fig. 7(b)); this may point to concentration-dependent quenching, but its mechanism cannot be established from the present data. From the present PL spectra, it is clear that the emission profile is strongly dependent on excitation wavelength.

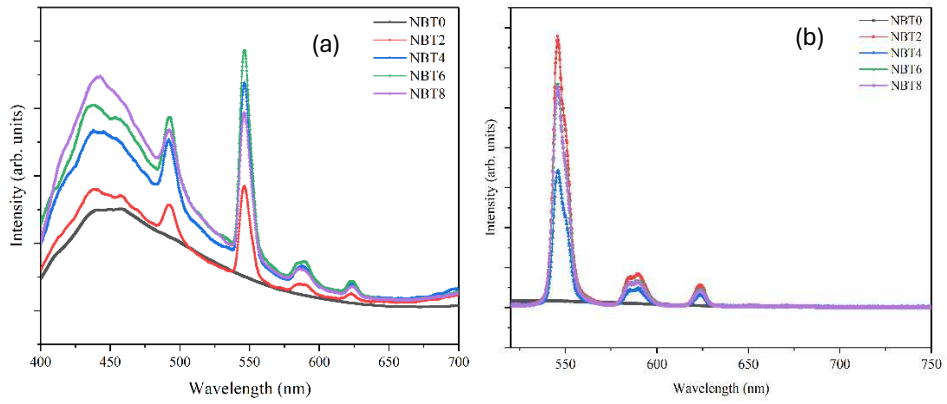


Fig. 7 PL spectra of $Na_{0.5}(Bi_{1-x}Tb_x)_{0.5}TiO_3$, excited with wavelength 378 nm (a) and 488nm (b)

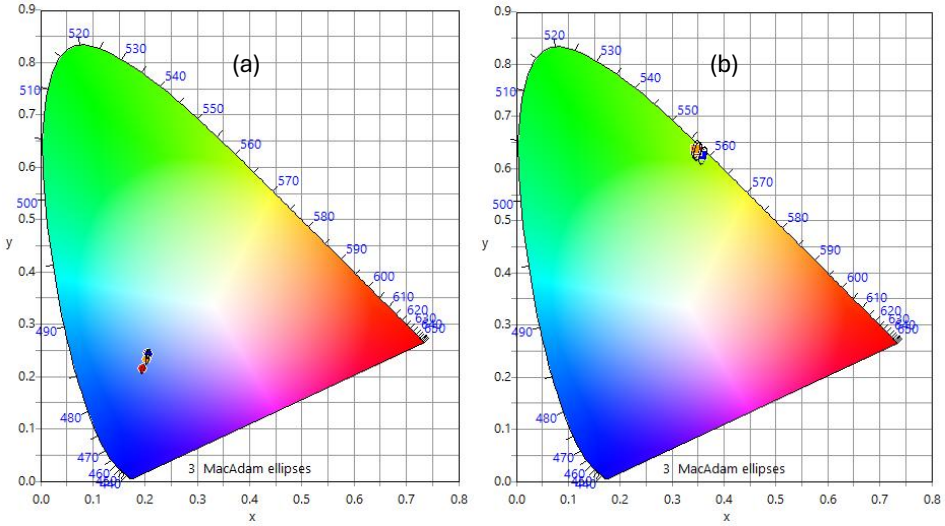


Fig. 8 The (x, y) emissive of NBT2 → NBT8 upon the (a) 378 nm and (b) 488 nm excitations

The emissive colors of the investigated samples under 378 nm and 488 nm excitations were evaluated in terms of the (x, y) color coordinates using the OSRAM Color Calculated software [24]. Under 378 nm, the (x, y) values are *(0.2055, 0.2431), (0.2066, 0.2426), (0.1956, 0.2140),* and *(0.2043, 0.2325)* for x = 0.02, 0.04, 0.06, and 0.08, respectively. Under 488 nm excitation, the (x, y) values for these samples are *(0.3495, 0.6328), (0.3594, 0.6250), (0.3498, 0.6331),* and *(0.3460, 0.6362)*. These (x, y) values under 378 nm and 488 nm excitations are depicted in Fig. 8. As observed in Figure 8, the emissive color of samples strongly depend on excitation wavelength, from blue to green. The excitation-dependent shift from blue to green reflects the different excitation pathways: 378 nm, which can also excite the host, produces a broad host-related blue band together with Tb^{3+} emission ($^7F_6 \rightarrow {}^5G_6/{}^5D_3$, nonradiative relaxation to $^5D_4$, then $^5D_4 \rightarrow {}^7F_J$), whereas 488 nm excites Tb^{3+} directly via $^7F_6 \rightarrow {}^5D_4$ and yields green emission. This excitation-dependent color tunability suggests potential for excitation-selective optical tagging and anti-counterfeiting, although device-level demonstration was beyond the scope of the present work.

4 Conclusion

In this study, Tb^{3+} doped NBT ceramics were fabricated using conventional solid-state reaction method. The X-ray diffraction pattern confirmed the formation of a perovskite structure, while Rietveld refinement showed the average structure of all samples is well described by the *R3c* space group. SEM observations characterized the surface morphology and grain-size distribution, indicating a gradual decrease in grain size with increasing Tb^{3+} concentration. EDS confirmed the presence of Tb, while Raman spectroscopy revealed composition-dependent changes in the local vibrational environment consistent with Tb^{3+} substitution at the A site. Photoluminescence investigation demonstrated that emission spectra of Tb^{3+} doped samples contain peaks which correlate to the respective characteristic transitions $^5D_4 \rightarrow {}^7F_6$ (492 nm), $^5D_4 \rightarrow {}^7F_5$ (545 nm), $^5D_4 \rightarrow {}^7F_4$ (587 nm), and $^5D_4 \rightarrow {}^7F_3$(624 nm) of Tb^{3+} ions. Furthermore, the emission color depends on the excitation wavelength: a broad host-related blue band together with Tb^{3+} lines under 378 nm (CIE ≈ (0.20, 0.23)), and green Tb^{3+} emission under 488 nm (CIE ≈ (0.35, 0.63)). Overall, these findings highlight the relationship between structural evolution and excitation-dependent optical functionality in Tb^{3+} doped NBT, suggesting potential for excitation-tunable luminescent materials such as optical anti-counterfeiting labels.

Statements and Declarations

Funding

This research was supported by Ho Chi Minh City University of Technology and Engineering (HCM-UTE) under Grant No. T2026-15.

Competing interests

The authors declare no competing interests.

Author contributions

All authors contributed to the study conception and design. T.N. Dat and T.P. Hoang planned and supervised the work. L.V. Thanh Son, D.T. Khan, N.B.V. Chinh, P. Lien and L.V. Truong Son synthesized the samples and performed the XRD, SEM/EDS, Raman and photoluminescence measurements. T.A. Tran, L.S. Hai and T.T. Thanh-Thao carried out the data analysis and wrote the original draft of the manuscript. H.V. Truong, R.B. Jabbarov, S.H. Jabarov and Y.I. Aliyev contributed to the structural (Rietveld) and theoretical analysis, and reviewed and edited the manuscript. T.A. Tran acquired the funding. All authors discussed the results and approved the final manuscript.

Data availability

All data that support the findings of this study are included within the article (and any supplementary files).

References

1. S. Behara, K. Ikeda, T. Thomas, Ceram. Int. 47, 12870 (2021). https://doi.org/10.1016/j.ceramint.2021.01.149
2. A. Kumar, S. Asthana, J. Mater. Sci.: Mater. Electron. 32, 20225 (2021). https://doi.org/10.1007/s10854-021-06526-w
3. M.K. Niranjan, T. Karthik, S. Asthana, J. Pan, U.V. Waghmare, J. Appl. Phys. 113 (2013). https://doi.org/10.1063/1.4804940
4. M. Aissa, M. Teieb, J. Zidani, S. Dridi-Dhaouadi, H. Barhoumi, A. Lahmar, J. Alloys Compd. 1034 (2025). https://doi.org/10.1016/j.jallcom.2025.181043
5. S. Ye, F. Xiao, Y.X. Pan, Y.Y. Ma, Q.Y. Zhang, Mater. Sci. Eng. R Rep. 71, 1 (2010). https://doi.org/10.1016/j.mser.2010.07.001
6. K.R. Kandula, S. Asthana, S.S.K. Raavi, RSC Adv. 8, 15282 (2018). https://doi.org/10.1039/c8ra01349g
7. Q. Yao, F. Wang, F. Xu, C.M. Leung, T. Wang, Y. Tang et al., ACS Appl. Mater. Interfaces 7, 5066 (2015). https://doi.org/10.1021/acsami.5b00420
8. C. He, Y. Zhang, L. Sun, J. Wang, T. Wu, F. Xu et al., J. Phys. D Appl. Phys. 46, 245104 (2013). https://doi.org/10.1088/0022-3727/46/24/245104
9. S. Swain, B. Ojha, S. Mohanty, J. Mater. Sci.: Mater. Electron. 27, 8693 (2016). https://doi.org/10.1007/s10854-016-4891-9
10. A. Jeshurun, Irfan Mohammad, S. Behara, M.R. Bogala, Mater. Today Chem. 20 (2021). https://doi.org/10.1016/j.mtchem.2021.100476
11. W.G. Wang, X.Y. Li, T. Liu, G.L. Hao, Solid State Ion. 290, 6 (2016). https://doi.org/10.1016/j.ssi.2016.03.023

12. Y. Yuan, C.J. Zhao, X.H. Zhou, B. Tang, S.R. Zhang, J. Electroceram. 25, 212 (2010). https://doi.org/10.1007/s10832-010-9617-4
13. L. Cui, C. Di, T. Wang, B. Xie, J. Qiu, J. Guo et al., J. Power Sources 689, 240773 (2026). https://doi.org/10.1016/j.jpowsour.2026.240773
14. S. Behara, R. Hari Krishna, M. Muralidhar, M. Murakami, M. Irfan, S. Najma et al., Materialia 7, 100426 (2019). https://doi.org/10.1016/j.mtla.2019.100426
15. S. Mohanty, R.N.P. Choudhary, J. Mater. Sci.: Mater. Electron. 25, 1180 (2014). https://doi.org/10.1007/s10854-014-1706-8
16. A. Shukla, R.N.P. Choudhary, A.K. Thakur, J. Phys. Chem. Solids 70, 1401 (2009). https://doi.org/10.1016/j.jpcs.2009.08.015
17. K. Parmar, N.S. Negi, J. Alloys Compd. 618, 781 (2015). https://doi.org/10.1016/j.jallcom.2014.07.138
18. S. Kaur, N. Deopa, A. Prasad, R. Bajaj, A.S. Rao, Opt. Mater. 84, 318 (2018). https://doi.org/10.1016/j.optmat.2018.07.020
19. C. Sumalatha, R. Doddoji, M. Venkateswarlu, K. Swapna, S.K. Mahamuda, A.S. Rao, Radiat. Phys. Chem. 208, 110894 (2023). https://doi.org/10.1016/j.radphyschem.2023.110894
20. P. Du, Y. Hua, J.S. Yu, RSC Adv. 8, 26676 (2018). https://doi.org/10.1039/c8ra05284k
21. Y. Lin, C.-W. Nan, J. Wang, H. He, J. Zhai, L. Jiang, Mater. Lett. 58, 829 (2004). https://doi.org/10.1016/j.matlet.2003.07.025
22. Y. Huang, L. Luo, J. Alloys Compd. 706, 312 (2017). https://doi.org/10.1016/j.jallcom.2017.02.141
23. Y. Cai, K. Ren, H. Ding, Y. Zhang, J. Alloys Compd. 1044, 184453 (2025). https://doi.org/10.1016/j.jallcom.2025.184453
24. D.T. Khan, N.T. Dang, S.H. Jabarov, T.G. Naghiyev, R.M. Rzayev, T.Q. Nguyen et al., Mater. Res. Express 7, 016507 (2020). https://doi.org/10.1088/2053-1591/ab5ab8